Research Article Vol. 3, No. 2 / 25 April 2025 / Optica Quantum 175

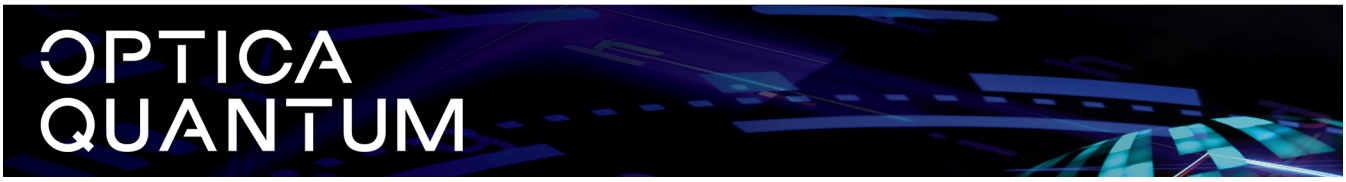

Cavity enhancement of V2 centers in 4H-SiC with a fiber-based Fabry–Perot microcavity

Jannis Hessenauer,[1,†,*] Jonathan Körber,[2,8,†] Misagh Ghezellou,[3] Jawad Ul-Hassan,[3] Georgy V. Astakhov,[4] Wolfgang Knolle,[5] Jörg Wrachtrup,[2,6] and David Hunger[1,7]

[1]Physikalisches Institut, Karlsruhe Institute of Technology (KIT), Wolfgang-Gaede-Str. 1, 76131 Karlsruhe, Germany
[2]3rd Institute of Physics, University of Stuttgart, Allmandring 13, 70569 Stuttgart, Germany
[3]Department of Physics, Chemistry and Biology, Linköping University, 581 83 Linköping, Sweden
[4]Institute of Ion Beam Physics and Materials Research, Helmholtz-Zentrum Dresden-Rossendorf, 01328 Dresden, Germany
[5]Leibniz-Institute of Surface Engineering (IOM), Permoserstraße 15, 04318 Leipzig, Germany
[6]Max Planck Institute for Solid State Research, Heisenbergstraße 1, 70569 Stuttgart, Germany
[7]Institute for Quantum Materials and Technologies (IQMT), Karlsruhe Institute of Technology (KIT), Herrmann-von-Helmholtz Platz 1, 76344 Eggenstein-Leopoldshafen, Germany
[8]jonathan.koerber@pi3.uni-stuttgart.de
[†]The authors contributed equally to this work.
[*]jannis.hessenauer@kit.edu

Received 17 January 2025; revised 3 March 2025; accepted 3 March 2025; published 28 March 2025

Silicon vacancy centers in 4H-silicon carbide (SiC) host a long-lived electronic spin with spin-resolved optical transitions. This makes them a great candidate for implementing a spin–photon interface, an important building block of quantum networks. However, the fraction of coherently scattered photons is intrinsically low, limiting the achievable communication rates. To address this problem, we integrate V2 centers within a SiC membrane into a fiber-based Fabry–Perot microcavity. We find that SiC is uniquely suited for this approach, offering extremely low losses as we evidence by a high cavity finesse $\mathcal{F} \approx 40\,000$ and naturally available maximal cavity–emitter coupling due to the perfect alignment of polarization modes and the dipole orientation. We observe a 13.3-fold Purcell enhancement of the zero phonon line of a single emitter, constituting an efficient source of coherent photons for this novel material platform, and opening the path toward a deterministic spin–photon interface.

https://doi.org/10.1364/OPTICAQ.557206

1. INTRODUCTION

Spin-active quantum emitters in solids are considered a promising platform for quantum technology applications [1,2]. Diamond, as the main host material for such emitters, has been used for pioneering experiments in the field [3–8]. However, other semiconductor materials such as silicon (Si) [9–11] and silicon carbide (SiC) [12,13] have recently gained increasing attention because they offer advantages such as complementary metal-oxide-semiconductor (CMOS)-fabrication compatibility and wafer-scale material availability [14–17] while still hosting promising quantum emitters, such as silicon-vacancy centers (V_{Si}) [18–20] or divacancy centers (VV) [21–23] in 4H-SiC. The VSi-center in 4H-SiC has already been used for encouraging demonstrations of single-shot readout of the spin state for the k-site VSi (V2) [24,25] and spin–photon entanglement for the h-site VSi (V1) [26]. However, it shows only low Debye–Waller factors (6 % to 9 %) and a moderate quantum efficiency of $QE = 28.6\%$, thus raising challenges for useful quantum technology applications with the system [27–30].

Different photonic structures have already been demonstrated to enhance the collected photon rate [31–36]. Yet, to specifically enhance the zero-phonon line (ZPL) transition of the emitters, highly resonant structures that can harness the Purcell effect must be used. This increases the rate of coherent photons, which are necessary to generate and distribute remote entanglement in quantum networks [2]. Photonic crystal cavities and disk resonators have already been used to enhance V_{Si}- and VV-centers in 4H-SiC [37–39]. Compared with these integrated structures, open microcavities such as (fiber-based) Fabry–Perot cavities offer the possibility of easy tunability of the spatial and spectral position of the cavity resonance [40–43]. This enables the *in situ* optimization of resonance conditions and the investigation of multiple emitters with a single cavity. With this approach, emitters can be integrated within thin membranes bonded onto the cavity mirror, as already successfully demonstrated for the diamond platform [44–49]. Crucially, this allows one to position emitters farther from surfaces, avoiding spectral diffusion due to charge fluctuations.

In this work, we demonstrate the coupling of V2 centers inside a few-micrometer-thin 4H-SiC membrane to a fiber-based Fabry–Perot cavity. We produce two membranes with an extremely low surface roughness of 350 pm to 400 pm root mean square (r.m.s.) and high spatial homogeneity. We study the losses and dispersion of the cavity–membrane system and find excellent agreement with theoretical descriptions and simulations, as well as minimal loss introduced by the membrane, for both samples. We then analyze the emitter properties and find a reduced lifetime when resonant with the cavity due to the Purcell effect. Finally, we show that by using the cavity to spectrally select individual emitters, we achieve high single-photon purity and high ZPL count rates.

2. RESULTS AND DISCUSSION

2.1. Sample Fabrication and Characterization

The samples we use for our experiments are made from a commercial, n-type, a-plane 4H-SiC wafer (Wolfspeed) with a 10 µm-thick high-quality epilayer grown on the top side. In total, we fabricate and investigate two samples: sample A (SA) and sample B (SB). Analogously to previous work [36,50], we use a series of lapping and chemical–mechanical polishing (CMP) to thin the samples from the wafer side down to a total thickness of ∼40 µm. Subsequently, the samples are van der Waals bonded with the epilayer side onto a commercially coated distributed-Bragg-reflector (DBR)-mirror (Laseroptik), using an oxygen plasma activation (see Supplement 1 for details on the bonding procedure). Next, we thin the samples on the mirror further down to a few-micron-thin membranes using a SF_6-based reactive-ion etching (RIE) process. In order to prevent a strong amount of micromasking due to nonvolatile etch by-products from the mirror and to preserve parts of the free mirror throughout the etching, we use a SiC hard mask with a square opening on top of the silicon carbide sample SA and only etch it within the opening of the mask. This yields only a square sub-region of the whole SiC sample at the target thickness as visible in the microscope image of Fig. 1(a). The SB is etched without a hard mask on top. Our etching leaves the surface with a low r.m.s. roughness of ∼400 pm (see Supplement 1 for AFM measurements), which is crucial for high-finesse cavity experiments. To create V2-centers, we use electron irradiation at an energy of 5 MeV and a dose of 5 kGy (see Supplement 1 for more information on the electron irradiation and for a full process flow diagram of the fabrication).

To confirm the presence of V2 centers in the fabricated samples, we use a home-built confocal microscope at room temperature (*NA* = 0.9 objective). Figure 1(b) shows a typical fluorescence map of a central region within the membrane SA under off-resonant excitation at 785 nm. Since the V2 emission spectrum has no characteristic peak at room temperature, we use optically detected magnetic resonance (ODMR) measurements to identify V2 centers together with a preselection based on the polarization of the fluorescence (see Ref. [36] for details on the preselection). Out of 14 preselected spots, we find eight that show a clear ODMR signal from a V2 center (see Supplement 1 for details on the ODMR measurements). The remaining six spots are most likely V1 centers.

To characterize the optical properties of the V2 centers in SA, we cool the sample to 8 K in a closed-cycle cryostat (Montana Instruments), and use a second home-built confocal

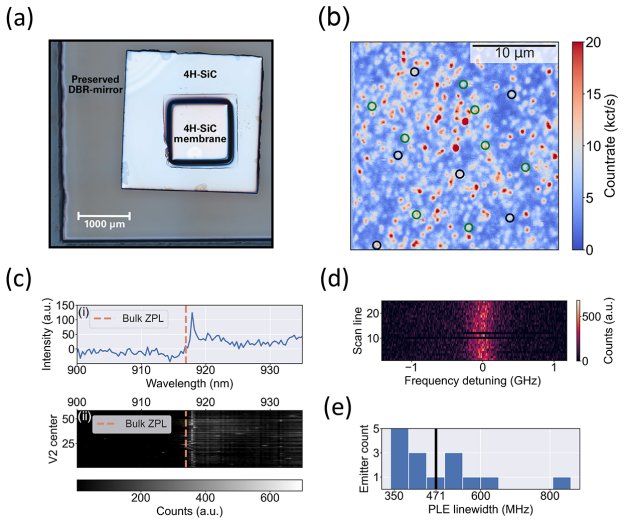

Fig. 1. Fabrication and characterization of the membrane SA. (a) Light microscope image of the sample after the fabrication. (b) Room temperature confocal fluorescence scan in the membrane region of the sample. Diffraction limited spots that were further investigated by ODMR are marked with a circle. The green circles show spots with a clear ODMR signature from a V2 center. (c) Background corrected emission spectrum of (i) a single spot under off-resonant excitation and integration for 20 s at a temperature of 8 K and (ii) spectra of 58 investigated V2 centers stacked above each other. The orange, dashed line indicates the ZPL position from bulk V2 centers. (d) The PLE scans of a single V2 center in the membrane at 8 K. The two dark lines are due to an ionization of the emitter upon resonant excitation. (e) The PLE-linewidth distribution of different V2 centers in the membrane. The linewidth is extracted by the average full-width half-maximum (FWHM) of Lorentzian fits on 25 single-line PLE scans for each center. The black solid line at 471 MHz depicts the average linewidth of all investigated V2 centers.

microscope (*NA* = 0.75 objective) for cryogenic spectroscopy. Here, we identify V2 centers from their emission spectra under off-resonant excitation at 730 nm, as shown for an exemplary emitter in Fig. 1(c i). Compared with the ZPL of the bulk centers at 917 nm [27,51], we find that the ZPLs of most emitters in the bonded membrane are shifted by ∼1 nm, as depicted in the stacked spectra plot of 58 different emitters in Fig. 1(c ii). We attribute this shift to a homogeneous strain inside the sample arising from the bonding to the DBR-mirror: a ZPL shift of 1 nm could be explained by strain of 0.02 % parallel to the c-axis [27], which is a realistic amount since similar strain has been already observed for bonded SiC as a consequence of lattice mismatch [52].

Finally, we investigate the linewidths of the optical transitions of membrane-integrated V2 centers by photoluminescence excitation (PLE) scans. As described in earlier work [36], we use acousto-optic modulators (AOMs) to generate a laser beam containing two wavelengths split by 1 GHz. With this beam, we simultaneously scan over both optical transitions of the V2 center at a power of 5 nW before the objective and collect the photons from the phonon sideband (PSB). Figure 1(d) shows a series of such scans from the same emitter stacked over each other with no visible spectral jumps. To evaluate the linewidth, we fit a Lorentzian to each individual line and extract the mean linewidth from the series. We repeat these

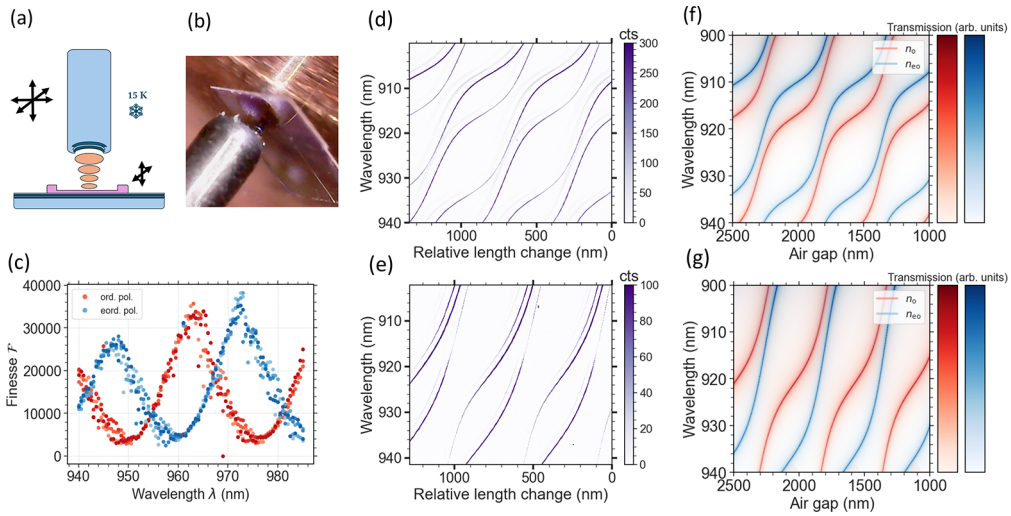

Fig. 2. Characterization of the membrane cavity system. (a) Schematic sketch of the fiber-cavity–membrane system. (b) Photograph of the fiber mirror protruding from a metallic needle opposing the membrane bonded onto a planar DBR mirror. (c) Finesse as a function of wavelength for two orthogonal polarizations, corresponding to the ordinary and extraordinary polarization modes of the SiC membrane. The periodic modulation is due to the SiC membrane. (d),(e) Measured cavity dispersion of SA and SB, showcasing the characteristic hybridization of air-like and dielectric-like modes for membrane cavity systems. Due to the birefringence of SiC, we observe two families of modes. The different membrane thickness changes the periodicity of the mode coupling. The fainter, slightly offset traces correspond to higher-order cavity modes. (f),(g) Simulated dispersion for SA and SB. The simulation reproduces the measurements. Extracted membrane thicknesses are $d_{SA} = 6.20\,\mu m$ and $d_{SB} = 2.85\,\mu m$.

measurements for a total of 15 emitters and find a mean PLE linewidth of 471(132) MHz for all emitters, as depicted in Fig. 1(e). To exclude a significant power broadening of the optical linewidths, we perform excitation power-dependent PLE linewidth measurements on a single emitter and find that there is no significant power broadening at 5 nW excitation power (see Supplement 1). We note that the average PLE linewidth of 471(132) MHz appears to be higher than the linewidth reported from similar samples [36,50]. Possible explanations for the increased linewidth include non-perfect thermalization of the sample and an increased amount of charge noise, both stemming from the thick, isolating glass substrate of the mirror between the silicon carbide membrane and the copper plate inside the cryostat.

2.2. Cavity Characterization

In order to characterize the membrane–mirror system performance, we integrate the sample into a home-built positioning unit, forming a microcavity together with a fiber mirror that is approached closely to the membrane, as sketched in Fig. 2(a) and depicted in Fig. 2(b). The positioning setup is located in a closed-cycle cryostat as reported in an earlier work [53]. The fiber mirror can be scanned laterally across the mirror over a range of $20\,\mu m \times 20\,\mu m$ and the cavity length can be tuned over multiple free spectral ranges. This enables us to spatially search for emitters, optimize the lateral overlap of emitter and cavity mode and then minimize the cavity length by bringing the fiber mirror in contact with the membrane. The contact configuration has the added benefit of drastically improving the longitudinal stability. This allows us to avoid active stabilization and passively stay on resonance with the ZPL despite a relatively high finesse. This configuration is used for all fluorescence measurements in this work (data presented in Figs. 3 and 4).

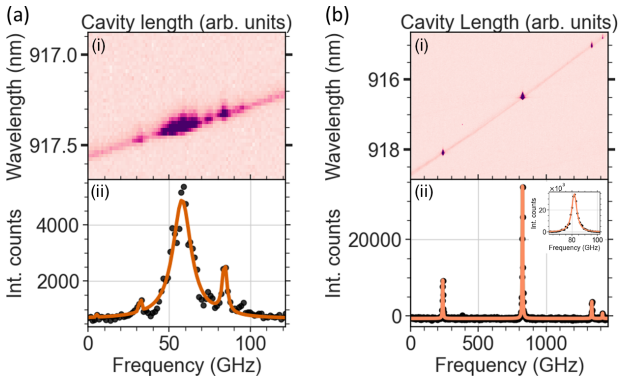

Fig. 3. Coupling of ZPLs to cavity modes. Cavity dispersion measured under off-resonant excitation. (a i,b i) A strong increase in emission is observed when the cavity is resonant with the ZPLs. (a ii,b ii) By integrating the individual spectra and calibrating the local dispersion, we can extract a frequency distribution of ZPLs. The orange line is a fit of multiple Lorentzians to the data. Notably, the thicker membrane (a) SA shows a denser and more centered distribution of emitters, while (b) SB exhibits sharp peaks with large spacings.

We begin by measuring the finesse at a small mirror distance by monitoring the transmission of a narrow linewidth laser through the cavity, while modulating the cavity length over multiple free spectral ranges. The transmission spectrum is fitted with Lorentzians to determine the positions and linewidths of the fundamental modes, allowing us to calculate the finesse. The finesse as a function of the probe wavelength is displayed in Fig. 2(c). It exhibits a strong dependence on the probe wavelength, due to the modulation of the DBR transmission by the membrane. The presence of a membrane in the cavity leads to the formation of a dielectric and air-like set of modes, see Refs.

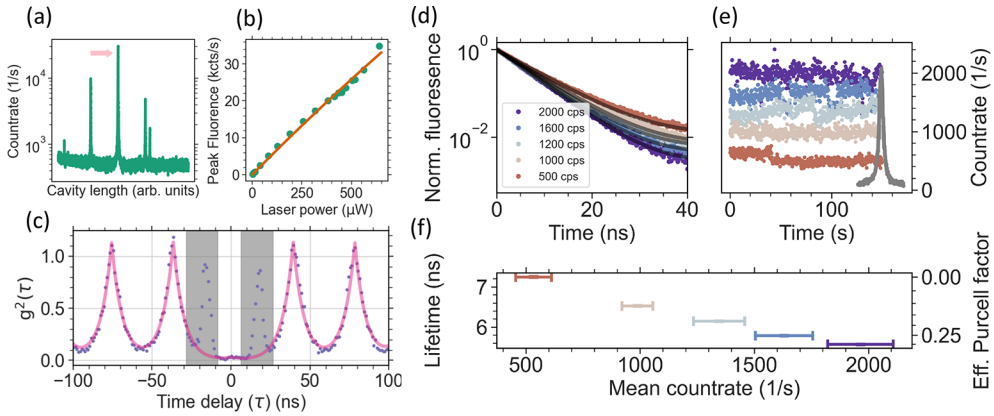

Fig. 4. Characterization of the emitter fluorescence in the cavity. (a) Detected count rate under off-resonant, pulsed excitation as a function of cavity detuning. At least four distinct peaks belonging to different ZPLs are visible. The brightest peak shows a ZPL count rate of 30 kcps. Note the close similarity to the measurement in Fig. 3(b), when accounting for the different y-axis scaling. (b) Excitation power dependence of the ZPL count rate under pulsed excitation. The laser power was measured behind the cavity. No clear saturation behavior was observed. (c) Pulsed auto-correlation measurement with the cavity resonant with the peak marked in (a), showcasing a high single-photon purity of $g^{(2)}(0) = 0.024(24)$ without background correction. Coincidence counts in the gray area arise from recombination photons in the counting photon avalanche diodes (APDs) and are excluded from the fit (see Supplement 1 for details). (d) Detuning dependent optical lifetime measurements of the resonance marked in (a). The detuning is reflected by the average count rate during the measurement. Solid lines show monoexponential fits with a constant offset to account for background counts. The count rate traces recorded during the lifetime measurement are plotted together with a sweep over the resonance in (e), in order to illustrate the cavity–emitter detuning and its stability. The lifetime reduces as the cavity becomes resonant with the ZPL, consistent with Purcell enhancement. The effective Purcell factors calculated from $C = \frac{\tau_0}{\tau} - 1$ are plotted in (f).

[54,55] and below. We observe a finesse as high as $\mathcal{F} = 40000$ at a wavelength of $\lambda = 980$ nm, which is almost twice the value observed for a bare cavity (see Supplement 1 for details on the coating). From simulations with a transfer matrix model, we can extract additional losses due to scattering and absorption in the high-finesse case of approximately $\mathcal{L}_{\text{air}} \approx 70$ ppm, further evidencing the high sample quality. We measure a finesse of up to $\mathcal{F} = 10000$ at $\lambda = 917$ nm, where the zero-phonon line of the V2 center is located.

Next, we measure the dispersion of the cavity–membrane system by coupling a broadband light source to the cavity and observing the resonances in transmission with a spectrometer, while stepwise changing the cavity length [Figs. 2(d) and 2(e)]. The mode hybridization of the cavity with the membrane manifests itself in a modulation of the cavity dispersion, as previously observed in comparable systems [44,47,55–57]. It is further complicated by the strong birefringence of 4H-SiC, which fully determines the polarization modes of the cavity and leads to two families of modes with orthogonal polarization [58]. The two polarization modes are also observed in the finesse measurement [Fig. 2(c)].

Simulated dispersion plots of the cavity membrane system using a transfer matrix model [44] are shown in Figs. 2(f) and 2(g). The good agreement with the experimental data confirms that our model captures the relevant effects and allows us to extract the membrane thickness of SA to be $d_{\text{SA}} = 6.2$ μm and of SB to be $d_{\text{SB}} = 2.85$ μm, in agreement with the measurements during fabrication using a profilometer.

2.3. Cavity Enhanced V2 Emission

We continue by measuring the properties of the emitters when coupled to the cavity. We couple an off-resonant diode laser ($\lambda = 785$ nm) to the cavity fiber to excite the emitters via the PSB. The mirror coating is almost transmissive at this wavelength, but still leads to a modulation of the intensity by a factor of ≈ 3, which we account for by measuring the excitation laser power after the cavity. We use filters to block the excitation light and detect the fluorescence in a spectral band of $\lambda = 900$–1000 nm, either using a spectrometer or two single-photon counters arranged in a Hanbury–Brown–Twiss (HBT) configuration.

First, we record spectra under off-resonant excitation while slowly varying the cavity length. Due to a broad background, we observe the cavity dispersion as in Figs. 2(d) and 2(e) as well as a strong increase in fluorescence when the cavity is resonant with the ZPL of one or more V2 centers (Fig. 3). Crucially, this is only observed for one polarization branch, because the dipole axis of the V2 center is oriented along the crystallographic c-axis, as is the extraordinary axis of the refractive index ellipsoid (see Supplement 1). This is useful for our application because it guarantees a maximal overlap between the emitter dipole and the cavity polarization, which otherwise would reduce the Purcell factor.

By performing these scans slowly and finely resolved, we note a substructure around the ZPL of SA [Fig. 3(a)], which we attribute to the inhomogeneous linewidth, originating from the different local electrical environment of multiple emitters. In our sample, multiple emitters are located inside the cavity mode waist, with the depth being randomly distributed. Thus, the lateral overlap and the position in the standing wave field, and therefore the coupling to the cavity mode and the observed peak count rate, vary for the different emitters. Interestingly, emitters in SB are both more sparse and spread over a larger frequency space [Fig. 3(b)]. Both facts can possibly be explained by the thinner membrane.

By fitting a linear slope to the local dispersion, we can calibrate the cavity length shift in terms of resonance frequency shift, allowing us to determine the feature linewidth by fitting

the calibrated integrated spectrum. The observed linewidth is a convolution of the linewidths of the cavity and the emitter. For sample SB, the brightest peak yields a linewidth of $\delta\nu = 4.8$ GHz, while the narrowest linewidth is obtained for the two rightmost peaks with $\delta\nu = 3.8$ GHz [Fig. 3(b ii)]. We measure the cavity linewidth at this position to be $\delta\nu_{\mathrm{cav}} = 3.44$ GHz by slowly (0.1 Hz) scanning a resonant laser over the cavity and recording the frequency with a wavemeter (see Supplement 1). This indicates a contribution from the emitter linewidth for the most dominant peak, which could be caused by insufficient thermalization of the mirror in the cavity stage. The temperature we measure at the mirror holder is 16 K. The linewidth of V2 centers is known to significantly increase above 20 K [27]. However, the sample is isolated from the copper mirror holder by the mirror substrate. To alleviate this, we add a copper link connecting the mirror holder to the sample, but a temperature gradient might nevertheless still persist.

Even though multiple emitters are located inside the cavity mode volume, we can make use of their inhomogeneous spectral distribution together with the spectral selectivity of the cavity to select individual emitters. In the thinner membrane SB, we observe peaks that are well isolated and are spread over a wide spectral range (915–918 nm). We set the cavity resonant with the brightest peak and measure the second-order autocorrelation $g^{(2)}(\tau)$ under pulsed off-resonant excitation (SuperK-Fianium, repetition rate 23.4 MHz, $\lambda = 780$–790 nm, $P = 230\,\mu$W). The measurement and a fit are displayed in Fig. 4(c). We observe a strong antibunching dip at $\tau = 0$ ns with $g^{(2)}(0) = 0.024(24)$, indicating a high single-photon purity. This underlines the ability of the cavity to spectrally select single emitters even under non-selective excitation, potentially enabling spectral multiplexing.

In order to quantify the achieved Purcell enhancement, we conduct lifetime measurements using the same pulsed laser source as above by recording the start-stop histograms between the laser emission and the detected photons. We vary the cavity emitter detuning and observe a lifetime-shortening as the cavity becomes resonant with the ZPL [see Figs. 4(d)–4(f)]. The shortest lifetime observed when the cavity and the emitter line coincide is $\tau_{\mathrm{min}} = 5.6$ ns. We take the longest lifetime observed for large detunings as the free space lifetime $\tau = 7.3$ ns, in good agreement with the values reported in the literature, e.g., $\tau = 7.08$ ns in Ref. [59]. The lifetime shortening allows us to determine the effective Purcell factor defined as $C_{\mathrm{eff}} = \frac{\tau_0}{\tau_{\mathrm{cav}}} - 1 = 0.30(1)$. The observed change in the lifetime is small because only the photons emitted into the narrow ZPL experience a significant Purcell enhancement, while all other decay channels remain unperturbed. Taking into account the fraction of coherently emitted photons via the Debye–Waller factor of DWF = 8% [27] and accounting for the quantum efficiency of QE = 28.6% [30], this corresponds to an ideal Purcell factor $C_0 = C_{\mathrm{eff}}/(\mathrm{DWF} \times \mathrm{QE}) = 13.3$. The ideal Purcell factor quantifies how many ZPL photons are additionally emitted into the cavity mode compared with free-space emission into 4π.

2.4. Discussion

For calculating the expected Purcell factor, we use the quality factor $Q = 7.4 \times 10^4$ extracted from the dispersion measurement [Fig. 3(b ii), inset], which is sensitive to both the linewidth of the cavity and the emitter. The mode volume $12.0\lambda_{\mathrm{V2}}^3$ is calculated by numerically integrating the field distribution obtained by the one-dimensional (1D)-simulation, yielding the effective cavity length $L_{\mathrm{eff}} = \frac{\int |n(z)E(z)|^2 \mathrm{d}z}{\max(n(z)E(z))}$. The mode volume is then given by $V = \frac{\pi w_0^2 L_{\mathrm{eff}}}{4}$, where the mode waist $w_0 = 1.66\,\mu$m in the membrane is calculated as previously reported in Refs. [44,54] by matching a Gaussian beam in the air gap to one in the membrane. This results in an expected Purcell factor of $C_0 = 25.7$. By using the quality factor obtained in the dispersion measurement, we automatically account for additional broadening of the emitters in the calculation, which could be caused by insufficient thermalization. Yet, the calculated value is almost twice as high as the observed Purcell enhancement. We believe that this difference can be explained by a non-perfect overlap of the defect with the cavity mode field, both transversally and longitudinally. Further, our calculations of the ideal Purcell factor depend on the literature values for the Debye–Waller factor and the quantum efficiency. While these properties have been studied carefully in the past, it is unclear how they are affected by a thin membrane, in particular because of applied stress.

However, even a relatively small lifetime reduction due to the small QE and DWF leads to a large increase of ZPL photons by a factor of C_0, which is confirmed by the observed ZPL count rates of up to 30 kcts/s [Fig. 4(a)]. We note that we use conventional silicon-based single photon counters, which feature a smaller detection efficiency (detection efficiency $\approx 30\%$) than the commonly used superconducting nanowire detectors (detection efficiency $\approx 90\%$). Furthermore, due to the limited available pulsed laser power and inefficient excitation due to the large cavity mode waist, we are unable to saturate the emitter. This is evident from both the saturation measurement depicted in Fig. 4(b) and the rather unpronounced bunching in $g^{(2)}(\tau)$ displayed in Fig. 4(c). We estimate that by driving the emitter in saturation, we could increase the count rate by at least a factor of four. Therefore, we predict that we can achieve more than an order of magnitude higher count rates by using a more potent laser source and state-of-the-art single photon detectors, without any changes to the cavity–membrane system.

3. CONCLUSION

In conclusion, we have demonstrated Purcell enhancement of single V2 centers in a few-micron-thick 4H-SiC membrane by integrating the membrane in a fiber-based Fabry–Perot cavity. The suitability of SiC for this approach is evident by the reproducible fabrication process, excellent surface roughness, and experimentally observed high finesse. We find a lifetime reduction of $C_{\mathrm{eff}} = 0.30$, which corresponds to a 13.3-fold enhancement of the coherent zero-phonon line. The spectral selectivity of the cavity allows us to achieve a high single-photon purity even though multiple defects are spatially located inside the cavity field. We detect up to 30 kcts /s ZPL photons from a single emitter, which could be increased by more than an order of magnitude by updating the experimental setup with state-of-the-art technology.

In future work, the Purcell factor could be increased by utilizing an optimized mirror coating with the stopband centered around the ZPL resonance. Operating an experiment with a finesse of $\mathcal{F} = 40\,000$, as measured in the center of the stopband for our mirror, requires extremely low cavity fluctuations, which, however, have been demonstrated for the setup used in this work using active stabilization. This would enable 10 times higher effective Purcell factors of up to $C_{\mathrm{eff}} = 3$. For spectrally narrow

emitters close to the lifetime limit, as already demonstrated for V2 centers in even thinner membranes [50], this corresponds to a cooperativity $C>1$, enabling spin-based reflection schemes which can be harnessed to generate remote entanglement [60]. Another important step forward is to demonstrate control of the spin state, either by integrating an RF line into the setup or by coherently driving the optical transitions.

Funding. Karlsruhe School of Optics and Photonics; Bundesministerium für Bildung und Forschung (16KISQ004, 16KIS1639K, Zukunftscluster Qsens); Deutsche Forschungsgemeinschaft (GRK2642); Baden-Württemberg Stiftung (QT-6); HORIZON EUROPE European Research Council (101135699, 731473, 101017733); Vetenskapsrådet (2020-05444).

Acknowledgements. We acknowledge fruitful discussions and experimental help from F. Kaiser, J. Heiler, K. Köster, S. Müller, M. Pallmann, R. Wörnle, T. Steidl, D. Liu, P. Kuna, and V. Vorobyov. G.A. gratefully acknowledges support from the Ion Beam Center (IBC) at HZDR for ion implantation.

Disclosures. The authors declare no conflicts of interest.

Data availability. The data to reproduce the figures in the main text are available at [61].

Supplemental document. See Supplement 1 for supporting content.

REFERENCES

1. M. Atatüre, D. Englund, N. Vamivakas, *et al.*, "Material platforms for spin-based photonic quantum technologies," Nat. Rev. Mater. **3**, 38–51 (2018).
2. D. D. Awschalom, R. Hanson, J. Wrachtrup, *et al.*, "Quantum technologies with optically interfaced solid-state spins," Nat. Photonics **12**, 516–527 (2018).
3. T. Gaebel, M. Domhan, I. Popa, *et al.*, "Room-temperature coherent coupling of single spins in diamond," Nat. Phys. **2**, 408–413 (2006).
4. G. Balasubramanian, I. Y. Chan, R. Kolesov, *et al.*, "Nanoscale imaging magnetometry with diamond spins under ambient conditions," Nature **455**, 648–651 (2008).
5. P. Neumann, J. Beck, M. Steiner, *et al.*, "Single-shot readout of a single nuclear spin," Science **329**, 542–544 (2010).
6. B. Hensen, H. Bernien, A. E. Dreaú, *et al.*, "Loophole-free Bell inequality violation using electron spins separated by 1.3 kilometres," Nature **526**, 682–686 (2015).
7. C. E. Bradley, J. Randall, M. H. Abobeih, *et al.*, "A ten-qubit solid-state spin register with quantum memory up to one minute," Phys. Rev. X **9**, 031045 (2019).
8. M. Pompili, S. L. Hermans, S. Baier, *et al.*, "Realization of a multinode quantum network of remote solid-state qubits," Science **372**, 259–264 (2021).
9. A. Durand, Y. Baron, W. Redjem, *et al.*, "Broad diversity of near-infrared single-photon emitters in silicon," Phys. Rev. Lett. **126**, 083602 (2021).
10. D. B. Higginbottom, A. T. Kurkjian, C. Chartrand, *et al.*, "Optical observation of single spins in silicon," Nature **607**, 266–270 (2022).
11. M. Hollenbach, N. Klingner, N. S. Jagtap, *et al.*, "Wafer-scale nanofabrication of telecom single-photon emitters in silicon," Nat. Commun. **13**, 7683 (2022).
12. S. Castelletto, A. Boretti, J. Phys Photonics, *et al.*, "Silicon carbide color centers for quantum applications," JPhys Photonics **2**, 022001 (2020).
13. S. Castelletto, A. Peruzzo, C. Bonato, *et al.*, "Silicon carbide photonics bridging quantum technology," ACS Photonics **9**, 1434–1457 (2022).
14. S. H. Ryu, K. T. Kornegay, J. A. Cooper, *et al.*, "Digital CMOS IC's in 6H-SiC operating on a 5-V power supply," IEEE Trans. Electron Devices **45**, 45–53 (1998).
15. J. Hassan, J. P. Bergman, A. Henry, *et al.*, "On-axis homoepitaxial growth on Si-face 4H-SiC substrates," J. Cryst. Growth **310**, 4424–4429 (2008).
16. G. Liu, B. R. Tuttle, and S. Dhar, "Silicon carbide: a unique platform for metal-oxide-semiconductor physics," Appl. Phys. Rev. **2**, 021307 (2015).
17. T. Yang, Y. Wang, R. Yue, *et al.*, "Demonstration of 4H-SiC CMOS digital IC gates based on the mainstream 6-inch wafer processing technique," J. Semicond. **43**, 082801 (2022).
18. H. Kraus, V. A. Soltamov, D. Riedel, *et al.*, "Room-temperature quantum microwave emitters based on spin defects in silicon carbide," Nat. Phys. **10**, 157–162 (2014).
19. M. Widmann, S. Y. Lee, T. Rendler, *et al.*, "Coherent control of single spins in silicon carbide at room temperature," Nat. Mater. **14**, 164–168 (2015).
20. R. Nagy, M. Niethammer, M. Widmann, *et al.*, "High-fidelity spin and optical control of single silicon-vacancy centres in silicon carbide," Nat. Commun. **10**, 1954 (2019).
21. N. T. Son, P. Carlsson, J. Ul Hassan, *et al.*, "Divacancy in 4H-SiC," Phys. Rev. Lett. **96**, 055501 (2006).
22. D. J. Christle, P. V. Klimov, C. F. de las Casas, *et al.*, "Isolated spin qubits in SiC with a high-fidelity infrared spin-to-photon interface," Phys. Rev. X **7**, 021046 (2017).
23. Q. Li, J. F. Wang, F. F. Yan, *et al.*, "Room-temperature coherent manipulation of single-spin qubits in silicon carbide with a high readout contrast," Natl. Sci. Rev. **9**, 1 (2022).
24. X.-Y. Lai, R.-Z. Fang, T. Li, *et al.*, "Single-shot readout of a nuclear spin in silicon carbide," Phys. Rev. Lett. **132**, 180803 (2024).
25. E. Hesselmeier, P. Kuna, W. Knolle, *et al.*, "High fidelity optical readout of a nuclear spin qubit in Silicon Carbide," Phys. Rev. Lett. **132**, 180804 (2024).
26. R.-Z. Fang, X.-Y. Lai, T. Li, *et al.*, "Experimental generation of spin-photon entanglement in silicon carbide," Phys. Rev. Lett. **132**, 160801 (2024).
27. P. Udvarhelyi, G. Thiering, N. Morioka, *et al.*, "Vibronic states and their effect on the temperature and strain dependence of silicon-vacancy qubits in 4H-SiC," Phys. Rev. Appl. **13**, 054017 (2020).
28. N. T. Son, C. P. Anderson, A. Bourassa, *et al.*, "Developing silicon carbide for quantum spintronics," Appl. Phys. Lett. **116**, 12 (2020).
29. Z. Shang, A. Hashemi, Y. Berencén, *et al.*, "Local vibrational modes of Si vacancy spin qubits in SiC," Phys. Rev. B **101**, 144109 (2020).
30. D. Liu, F. Kaiser, V. Bushmakin, *et al.*, "The silicon vacancy centers in SiC: determination of intrinsic spin dynamics for integrated quantum photonics," npj Quantum inf. **10**, 72 (2024).
31. M. Radulaski, M. Widmann, M. Niethammer, *et al.*, "Scalable quantum photonics with single color centers in silicon carbide," Nano Lett. **17**, 1782–1786 (2017).
32. F. Sardi, T. Kornher, M. Widmann, *et al.*, "Scalable production of solid-immersion lenses for quantum emitters in silicon carbide," Appl. Phys. Lett. **117**, 22105 (2020).
33. C. Bekker, M. J. Arshad, P. Cilibrizzi, *et al.*, "Scalable fabrication of hemispherical solid immersion lenses in silicon carbide through grayscale hard-mask lithography," Appl. Phys. Lett. **122**, 173507 (2023).
34. J. Y. Zhou, Q. Li, Z. H. Hao, *et al.*, "Plasmonic-enhanced bright single spin defects in silicon carbide membranes," Nano Lett. **23**, 4334–4343 (2023).
35. M. Krumrein, R. Nold, F. Davidson-Marquis, *et al.*, "Precise characterization of a waveguide fiber interface in silicon carbide," ACS Photonics **11**, 2160–2170 (2024).
36. J. Körber, J. Heiler, P. Fuchs, *et al.*, "Fluorescence enhancement of single V2 centers in a 4H-SiC cavity antenna," Nano Lett. **13**, 53 (2024).
37. A. L. Crook, C. P. Anderson, K. C. Miao, *et al.*, "Purcell enhancement of a single silicon carbide color center with coherent spin control," Nano Lett. **20**, 3427–3434 (2020).
38. D. M. Lukin, M. A. Guidry, and J. Vučković, "Integrated quantum photonics with silicon carbide: challenges and prospects," PRX Quantum **1**, 020102 (2020).
39. D. M. Lukin, M. A. Guidry, J. Yang, *et al.*, "Two-emitter multimode cavity quantum electrodynamics in thin-film silicon carbide photonics," Phys. Rev. X **13**, 011005 (2023).
40. D. Hunger, T. Steinmetz, Y. Colombe, *et al.*, "A fiber Fabry-Perot cavity with high finesse," New J. Phys. **12**, 065038 (2010).

41. C. Toninelli, Y. Delley, T. Stöferle, *et al.*, "A scanning microcavity for in situ control of single-molecule emission," Appl. Phys. Lett. **97**, 021107 (2010).
42. M. Mader, J. Reichel, T. W. Hänsch, *et al.*, "A scanning cavity microscope," Nat. Commun. **6**, 7249 (2015).
43. J. Fait, S. Putz, G. Wachter, *et al.*, "High finesse microcavities in the optical telecom O-band," Appl. Phys. Lett. **119**, 14 (2021).
44. E. Janitz, M. Ruf, M. Dimock, *et al.*, "Fabry-Perot microcavity for diamond-based photonics," Phys. Rev. A **92**, 043844 (2015).
45. D. Riedel, I. Söllner, B. J. Shields, *et al.*, "Deterministic enhancement of coherent photon generation from a nitrogen-vacancy center in ultrapure diamond," Phys. Rev. X **7**, 031040 (2017).
46. J. Heupel, M. Pallmann, J. Körber, *et al.*, "Fabrication and characterization of single-crystal diamond membranes for quantum photonics with tunable microcavities," Micromachines **11**, 1080 (2020).
47. M. Salz, Y. Herrmann, A. Nadarajah, *et al.*, "Cryogenic platform for coupling color centers in diamond membranes to a fiber-based microcavity," Appl. Phys. B **126**, 131 (2020).
48. M. Ruf, M. J. Weaver, S. B. Van Dam, *et al.*, "Resonant excitation and purcell enhancement of coherent nitrogen-vacancy centers coupled to a fabry-perot microcavity," Phys. Rev. Appl. **15**, 024049 (2021).
49. M. Pallmann, K. Köster, Y. Zhang, *et al.*, "Cavity-mediated collective emission from few emitters in a diamond membrane," Phys. Rev. X **14**, 041055 (2024).
50. J. Heiler, J. Körber, E. Hesselmeier, *et al.*, "Spectral stability of V2 centres in sub-micron 4H-SiC membranes," npj Quantum Mater. **9**, 1 (2024).
51. M. Wagner, B. Magnusson, W. M. Chen, *et al.*, "Electronic structure of the neutral silicon vacancy in 4H and 6H SiC," Phys. Rev. B **62**, 16555–16560 (2000).
52. I. D. Breev, K. V. Likhachev, V. V. Yakovleva, *et al.*, "Stress distribution at the AlN/SiC heterointerface probed by Raman spectroscopy," J. Appl. Phys. **129**, 55304 (2021).
53. M. Pallmann, T. Eichhorn, J. Benedikter, *et al.*, "A highly stable and fully tunable open microcavity platform at cryogenic temperatures," APL Photonics **8**, 046107 (2023).
54. S. B. Van Dam, M. Ruf, and R. Hanson, "Optimal design of diamond-air microcavities for quantum networks using an analytical approach," New J. Phys. **20**, 115004 (2018).
55. J. Körber, M. Pallmann, J. Heupel, *et al.*, "Scanning cavity microscopy of a single-crystal diamond membrane," Phys. Rev. Appl. **19**, 064057 (2023).
56. R. Høy Jensen, E. Janitz, Y. Fontana, *et al.*, "Cavity-enhanced photon emission from a single germanium-vacancy center in a diamond membrane," Phys. Rev. Appl. **13**, 064016 (2020).
57. J. Maisch, J. Grammel, N. Tran, *et al.*, "Investigation of Purcell enhancement of quantum dots emitting in the telecom O-band with an open fiber-cavity," Phys. Rev. B **110**, 165301 (2024).
58. P. Xing, D. Ma, K. J. Ooi, *et al.*, "CMOS-compatible PECVD silicon carbide platform for linear and nonlinear optics," ACS Photonics **6**, 1162–1167 (2019).
59. C. Babin, R. Stöhr, N. Morioka, *et al.*, "Fabrication and nanophotonic waveguide integration of silicon carbide colour centres with preserved spin-optical coherence," Nat. Mater. **21**, 67–73 (2022).
60. K. Nemoto, M. Trupke, S. J. Devitt, *et al.*, "Photonic architecture for scalable quantum information processing in diamond," Phys. Rev. X **4**, 031022 (2014).
61. J. Körber and J. Hessenauer, "Replication Data for 'Cavity enhancement of V2 centers in 4H-SiC with a fiber-based Fabry-Pérot microcavity'," DaRUS, 2025, https://doi.org/10.18419/DARUS-4788.